Supplementary Information: An NV^{-} center in magnesium oxide as a spin qubit for hybrid quantum technologies

Vrindaa Somjit,[1] Joel Davidsson,[2] Yu Jin,[3] and Giulia Galli[1,3,*]

[1]*Materials Science Division, Argonne National Laboratory, Lemont, IL 60439, USA*

[2]*Department of Physics, Chemistry and Biology,*
Linköping University, SE-58183, Linköping, Sweden

[3]*Pritzker School of Molecular Engineering and Department of*
Chemistry, University of Chicago, Chicago, IL 60637, USA

(Dated: February 08, 2025)

---

[*] gagalli@uchicago.edu

Supplementary Note 1. List of all 40 defects from ADAQ

Supplementary Tables 1 and 2 list the 40 defects and defect complexes on the defect hull with spin triplet ground state and zero-phonon line as found by ADAQ. Note that the first 11 defects in Supplementary Table 1 are listed in the main text. The last five defects in Supplementary Table 1 consist of cations on the oxygen site or anions on the magnesium site, and therefore will likely be challenging to realize experimentally.

Supplementary Table 1: Isolated defects and defect complexes of first nearest-neighbors on the defect hull with spin triplet ground state and zero-phonon line

Defect Type	Defect	Charge	ZPL [eV]	TDM [debye]	ΔQ [amu$^{1/2}$Å]
$\mathrm{X_O Vac_{Mg}}$	$\mathrm{B_O Vac_{Mg}}$	-1	0.5	1.93	1.45
	$\mathrm{I_O Vac_{Mg}}$	1	0.74	3.08	3.5
	$\mathrm{Sb_O Vac_{Mg}}$	-1	3.1	3.37	1.34
	$\mathrm{Bi_O Vac_{Mg}}$	-1	0.7	6.49	5.74
$\mathrm{X_{Mg} X_O}$	$\mathrm{B_{Mg} B_O}$	0	1.39	1.96	2.04
	$\mathrm{Al_{Mg} Al_O}$	0	0.68	1.35	1.0
	$\mathrm{Ga_{Mg} Ga_O}$	0	1.29	2.2	1.24
	$\mathrm{In_{Mg} In_O}$	0	0.98	2.7	1.2
	$\mathrm{Tl_{Mg} Tl_O}$	0	1.81	0.71	1.05
$\mathrm{X_O}$	$\mathrm{Ga_O}$	-1	4.19	6.16	0.58
$\mathrm{Int_X Vac_{Mg}}$	$\mathrm{Int_N Vac_{Mg}}$	-1	2.19	0.66	1.95
$\mathrm{X_O Int_O}$	$\mathrm{Ge_O Int_O}$	0	2.5	4.77	3.45
	$\mathrm{Sn_O Int_O}$	0	1.77	6.93	7.42
$\mathrm{I_X Vac_O}$	$\mathrm{I_{Mg} Vac_O}$	1	0.74	3.08	3.5
$\mathrm{X_{Mg} Int_X}$	$\mathrm{Br_{Mg} Int_{Br}}$	0	0.91	2.49	1.99
	$\mathrm{Cl_{Mg} Int_{Cl}}$	0	0.49	2.33	1.92

Supplementary Table 2: Isolated defects and defect complexes of second nearest-neighbors on the defect hull with spin triplet ground state and zero-phonon line

Defect Type	Defect	Charge	ZPL [eV]	TDM [debye]	ΔQ [amu$^{1/2}$Å]
$\mathrm{X_{Mg}Vac_{Mg}}$	$\mathrm{Rb_{Mg}Vac_{Mg}}$	-1	0.52	0.48	1.53
	$\mathrm{Ba_{Mg}Vac_{Mg}}$	0	0.47	2.14	1.18
	$\mathrm{H_{Mg}Vac_{Mg}}$	-1	2.43	1.85	1.44
	$\mathrm{O_{Mg}Vac_{Mg}}$	0	0.7	2.12	1.14
	$\mathrm{Cl_{Mg}Vac_{Mg}}$	-1	0.39	1.04	1.6
$\mathrm{X_{Mg}X_{Mg}}$	$\mathrm{H_{Mg}S_{Mg}}$	0	2.5	0.19	1.18
	$\mathrm{H_{Mg}S_{Mg}}$	0	0.87	5.26	1.53
$\mathrm{X_{Mg}X_{Mg}}$	$\mathrm{H_{Mg}S_{Mg}}$	0	2.5	0.19	1.18
	$\mathrm{H_{Mg}S_{Mg}}$	0	0.87	5.26	1.53
$\mathrm{X_{Mg}O_{Mg}}$	$\mathrm{I_{Mg}O_{Mg}}$	1	0.58	4.45	1.3
	$\mathrm{Bi_{Mg}O_{Mg}}$	-1	0.49	9.52	1.45
$\mathrm{X_{O}Mg_{O}}$	$\mathrm{Ga_{O}Mg_{O}}$	1	0.63	0	0.74
	$\mathrm{Li_{O}Mg_{O}}$	1	0.57	0.08	0.81
$\mathrm{X_{O}X_{O}}$	$\mathrm{N_{O}N_{O}}$	0	0.37	3.44	0.53
	$\mathrm{Ge_{O}Ge_{O}}$	0	0.63	0.23	1.09
	$\mathrm{Sn_{O}Sn_{O}}$	0	0.54	0.05	1.05
	$\mathrm{Si_{O}Si_{O}}$	0	0.68	0.17	0.93
	$\mathrm{Li_{O}Li_{O}}$	0	0.43	2.57	0.95
	$\mathrm{Mg_{O}Mg_{O}}$	0	0.2	7.38	0.82
	$\mathrm{Pb_{O}Pb_{O}}$	0	0.51	0.18	1.17
$\mathrm{X_{O}Vac_{O}}$	$\mathrm{Ca_{O}Vac_{O}}$	0	0.42	8.57	0.18
	$\mathrm{Sr_{O}Vac_{O}}$	0	0.39	7.86	1.06
	$\mathrm{Ga_{O}Vac_{O}}$	1	0.57	3.55	1.1
	$\mathrm{Al_{O}Vac_{O}}$	1	0.54	3.13	1.11
	$\mathrm{B_{O}Vac_{O}}$	1	0.99	2.39	0.96
	$\mathrm{Be_{O}Vac_{O}}$	0	0.38	6.22	0.98
	$\mathrm{Tl_{O}Vac_{O}}$	1	0.43	6.33	1.14

Supplementary Note 2. MgO band gap at different levels of theory and experiment

Supplementary Table 3 tabulates the MgO band gap at different levels of theory and experiment.

Supplementary Table 3: Computed band gaps of MgO at different levels of theory and experiment. Experimental band gap [1] includes zero-point renormalization [2].

	Band gap (eV)
PBE	4.47
DDH ($\alpha = 0.34$)	8.28
Experiment	8.36 [1, 2]

Supplementary Note 3. Stability of the NV complex vs. N_{Mg} substitutional defect

To check if the nitrogen interstitial can recombine with the magnesium vacancy to form a nitrogen substitutional defect on the magnesium site (N_{Mg}), we carried out DFT calculations at the DDH level for the N_{Mg}^{q} defect with different charge states q. We placed the nitrogen atom on the magnesium site and allowed all the ions to relax. We found that for $q = +1$, 0, and -1, the system relaxes to form the NV center (i.e., the nitrogen atom prefers to bond with an oxygen atom, instead of staying at the substitutional site). Thus, N_{Mg}^{-} is not stable and will always form the NV^{-} defect. For $q =$ -2, N_{Mg}^{2-} is higher in energy than the corresponding NV^{2-} defect by 0.07 eV; whereas for $q =$ -3, N_{Mg}^{3-} is higher in energy than the corresponding NV^{3-} defect by 2.52 eV. The reason for this can be understood from a molecular orbital analysis.

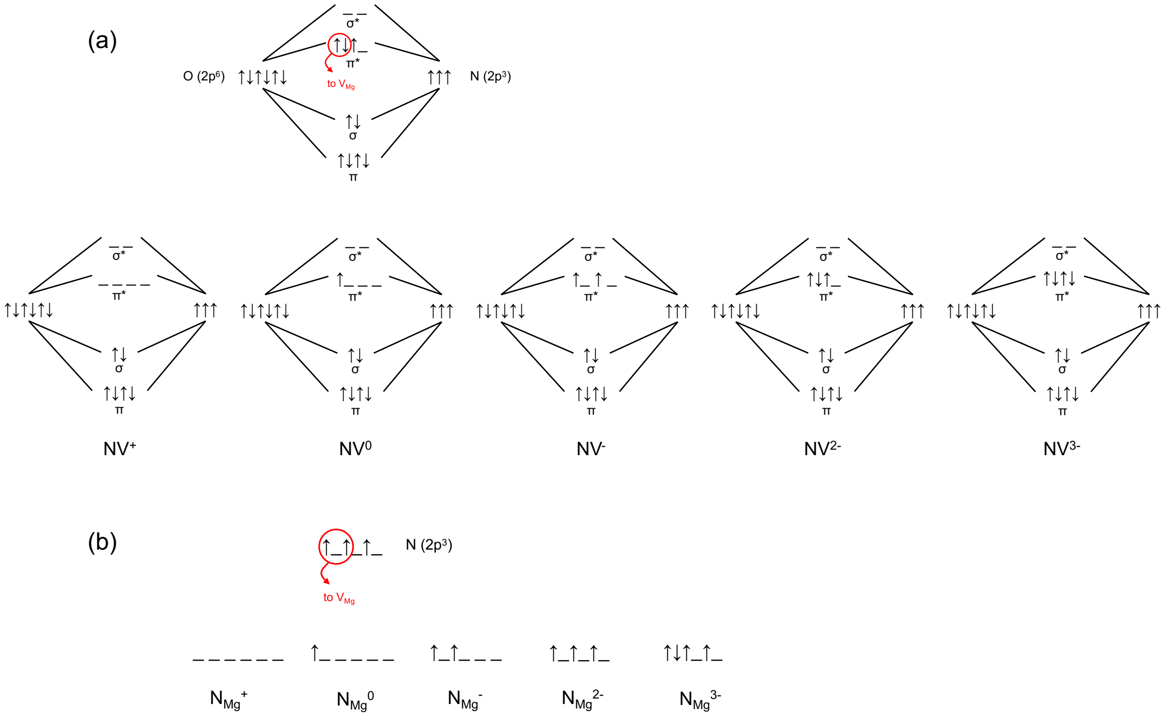

Supplementary Figure 1: a. Molecular orbital diagram for the NV defect with different charge states. The bonding orbitals formed from the p-orbitals of O^{2-} and N are shown. **b.** Orbital diagram from the N_{Mg} defect with different charge states. The nitrogen p-orbitals are shown.

Supplementary Figure 1a shows the molecular orbital diagrams for a nitrogen interstitial next to a magnesium vacancy (i.e., the NV defect), with different charge states q. When $q = 0$, the nitrogen atom ($2s^2 2p^3$) prefers to bond to the lattice O^{2-} ion ($2s^2 2p^6$) to form an N-O bond, resulting in the molecular orbital diagram shown in the top row of Supplementary Figure 1a. However, since the magnesium vacancy is an acceptor that can accept up to 2 electrons, 2 electrons from the π^* orbital are donated to the nearby magnesium vacancy. This gives us the NV^0 defect, with one electron in the π^* orbital. This also explains why the NV^- defect has a triplet ground state- the additional electron will prefer to occupy the spin up state of the π^* orbital following Hund's rule. The different charge states of the NV^q defect are shown at the bottom row of Supplementary Figure 1a.

Supplementary Figure 1b shows the orbital diagrams for a nitrogen substitutional on a magnesium site, with different charge states (q). This can be considered as a nitrogen atom on a magnesium vacancy. When $q = 0$, the nitrogen atom has the electron configuration $2s^2 2p^3$. Once again, since the magnesium vacancy is an acceptor that can accept up to 2 electrons, 2 electrons from the p-orbital of N are donated to the magnesium vacancy. This gives us the N_{Mg}^0 defect, with one electron in the p-orbital. However, the NV^0 configuration is preferentially formed, due to energetic stabilization from the formation of the N-O bond. This N-O bond formation is what promotes the formation of NV^+, NV^0, and NV^-, instead of the corresponding N_{Mg}^+, N_{Mg}^0, and N_{Mg}^-. However, N_{Mg}^{2-} is nearly as stable as NV^{2-}, likely due to the stability of the half-filled p-orbital on N in N_{Mg}^{2-}. For the same reason, NV^{3-} is much more stable than N_{Mg}^{3-}, due to the fully-filled π^* molecular orbital in NV^{3-}.

Supplementary Note 4. Migration barrier calculations

We computed the energy barrier for the nitrogen interstitial to migrate from one interstitial site to another interstitial site in the vicinity of the magnesium vacancy using the climbing image nudged elastic band method [3] (216 atom supercell, plane-wave cutoff of 80 Ry, Γ-point sampling, DDH functional). Supplementary Figure 2a plots the minimum energy pathway for nitrogen migration, and Supplementary Figure 2b shows the initial, saddle point, and final configurations. The computed migration barrier is 1.37 eV. Thus, once formed, this defect is expected to be stable against annealing.

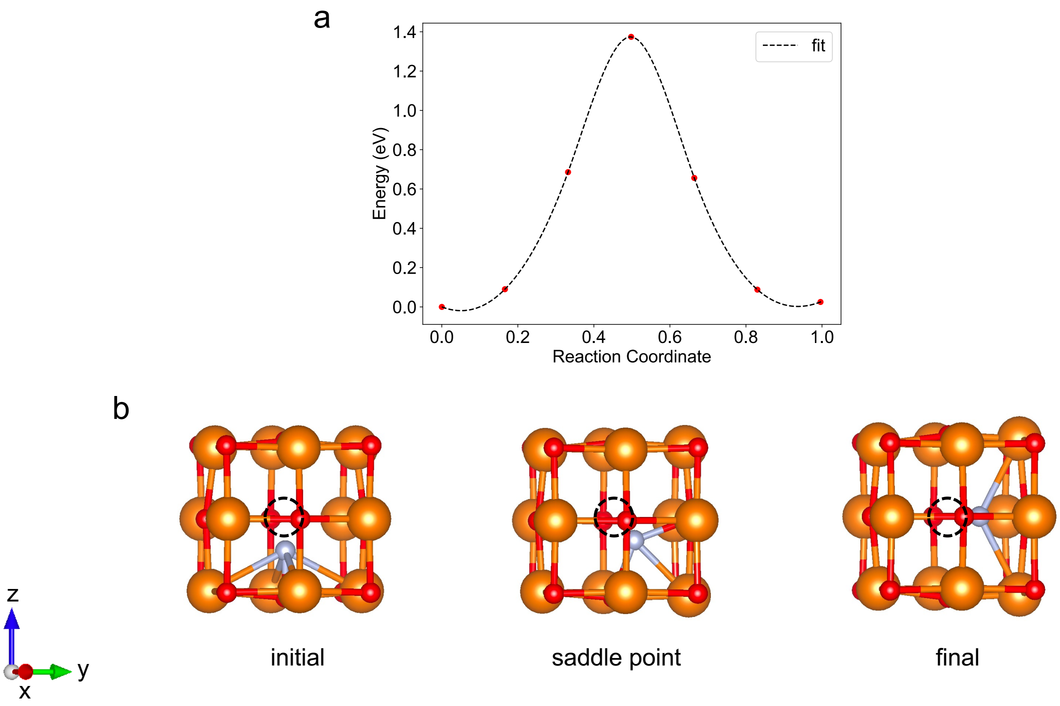

Supplementary Figure 2: **a.** Minimum energy pathway for the migration of the nitrogen interstitial from one side of the magnesium vacancy to another. **b.** Initial, saddle point, and final configurations.

Supplementary Note 5. Hyperfine interaction parameters of nitrogen defects in MgO

Supplementary Table 4 compares the hyperfine interaction parameters of various nitrogen defects in MgO. Note how the reported hyperfine parameters for substitutional nitrogen on the oxygen site and interstitial nitrogen are different from our calculated values for the NV^- defect.

Supplementary Table 4: Computed principal values of the hyperfine tensors for different nitrogen defects in MgO at the PBE level of theory (in G).

Atom	A_{xx}	A_{yy}	A_{zz}
N atom in NV^- defect[a]	15.55	15.55	-31.10
O atom bonded to N in NV^- defect[a]	-9.94	-9.95	19.89
N substitution on O site[b]	-11.9	-11.9	23.8
N interstitial[b]	-11.8	-11.3	23.2
O atom bonded to N interstitial[b]	15.2	15.3	-30.5

[a] This work

[b] Ref. [4]

Supplementary Note 6. Construction of the configuration coordinate diagram

The character table for the C_{4v} point group is given in Supplementary Table 5. The E electronic states can couple linearly to a_1, a_2, b_1, b_2 phonon modes, and to e phonon modes via higher (even) order coupling. However, symmetry can be broken only by the b_1, b_2, and e phonon modes. The optimized geometry of the ^3E excited state belongs to the C_1 point group, thus, e phonon modes must be predominant in reducing the symmetry from the C_{4v} point group to C_1.

Supplementary Table 5: Character table for C_{4v} point group

$\mathrm{C_{4v}}$	E	$\mathrm{2C_4(z)}$	$\mathrm{C_2}$	$2\sigma_\mathrm{v}$	$2\sigma_\mathrm{d}$	linear functions, rotations	quadratic functions	cubic functions
$\mathrm{A_1}$	+1	+1	+1	+1	+1	z	x^2+y^2, z^2	$z^3, z(x^2+y^2)$
$\mathrm{A_2}$	+1	+1	+1	-1	-1	R_z	-	-
$\mathrm{B_1}$	+1	-1	+1	+1	-1	-	x^2-y^2	$z(x^2-y^2)$
$\mathrm{B_2}$	+1	-1	+1	-1	+1	-	xy	xyz
E	+2	0	-2	0	0	$(x,y)(R_x,R_y)$	(xz,yz)	$(xz^2,yz^2)(xy^2,x^2y)(x^3,y^3)$

There are four equivalent minima with C_1 point symmetry. To verify that the e phonon modes are indeed predominantly involved in symmetry-breaking in the first excited ^3E state, we calculated the Mg, O, and N displacements between the average structure of the four equivalent minima and the optimized excited state structure. The average structure has contributions from only the a_1-phonon modes (as contributions from the symmetry-breaking modes cancel out, since they are equal in magnitude but opposite in direction for the four equivalent minima); therefore, the displacement between the average structure and the optimized excited state structure reveals the predominant symmetry-breaking mode.

Supplementary Table 6: Displacement components of the N atom, and O and Mg atoms nearest neighbor to the N atoms along the x-, y-, and z- directions. Unit is Å.

	Between average and ground state structures			Between excited state and average structures		
	$\mathrm{x_{es}} - \mathrm{x_{gs}}$	$\mathrm{y_{es}} - \mathrm{y_{gs}}$	$\mathrm{z_{es}} - \mathrm{z_{gs}}$	$\mathrm{x_{es}} - \mathrm{x_{gs}}$	$\mathrm{y_{es}} - \mathrm{y_{gs}}$	$\mathrm{z_{es}} - \mathrm{z_{gs}}$
$\mathrm{Mg_1}$	0.04	3.35e-05	7.98e-03	-0.08	5.82e-06	1.11e-03
$\mathrm{Mg_2}$	-3.34e-05	0.04	7.98e-03	9.54e-03	0.10	0.05
$\mathrm{Mg_3}$	-0.04	-3.34e-05	7.98e-03	0.13	-2.67e-04	-0.10
$\mathrm{Mg_4}$	3.35e-05	-0.04	7.98e-03	9.27e-03	-0.10	0.05
N	0	0	-0.39	0.51	1.70e-04	-2.92e-07
O	0	0	-0.13	-0.34	-4.15e-05	-1.86e-07

Supplementary Table 6 lists the displacement values between the average structure and the ground state structure, and the excited state structure and the average structure, for the N atom, and the O and Mg atoms nearest neighbor to the N atom. We find that a_1-phonon modes are predominant in generating the average structure (from the ground state structure), and e-modes are predominant in generating the optimized geometry in the excited state (from the average structure). We compared the observed phonon modes to the vibrational modes reported for the $\mathrm{XeOF_4}$ molecule [5], which has C_{4v} symmetry and a geometry similar to that of the $\mathrm{NV^-}$ defect center. The a_1-phonon mode is akin to the 'out of plane bend' mode, and the e-phonon mode is the 'bend' mode. Supplementary Figure 3 shows the ground state, average, and excited state structures, and the predominant phonon modes involved in each structure.

Thus, to calculate the vibronic coupling of the E electronic states with the e phonon modes, we take the average structure as the reference configuration for our configuration coordinate diagram (CCD), and interpolate points between this new reference configuration and one of the minima. This eliminates the influence of a_1-phonon modes (which are not Jahn-Teller or pseudo Jahn-Teller active) and gives the coupling of the E-states exclusively to the e-modes.

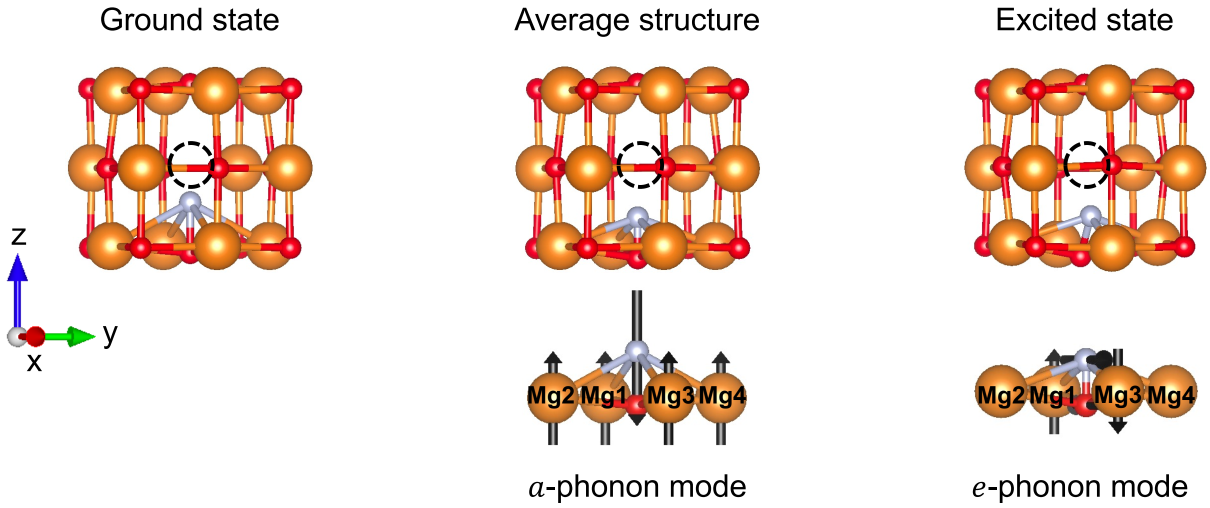

Supplementary Figure 3: **Top row**: Optimized geometry of the ground state structure, average structure of the four equivalent excited state minima, optimized geometry of the ^3E excited state (i.e. one of the four equivalent minima). **Bottom row**: predominant phonon modes involved in generating the average structure (from the ground state geometry) and the excited state structure (from the average structure). The displacement vectors for Mg_1, Mg_2, Mg_3, Mg_4 of the a-phonon modes are shown only along the z-direction and are scaled up by 38 times for clarity. Similarly, the displacement vectors for Mg_1 and Mg_3 of the e-phonon modes are scaled by 300 and 3 times respectively.

Supplementary Note 7. Construction of the adiabatic potential energy surface

To construct the adiabatic potential energy surface (APES) of the ^3E electronic state along the e-phonon mode and obtain the effective phonon frequencies and vibronic coupling constants, we followed the method proposed in [6] and [7]. We extended their method (which was developed for a C_{3v} $E\otimes e$ Jahn-Teller system [6] and a C_{3v} $(A+E)\otimes e$ pseudo Jahn-Teller system [7]) to our C_{4v} $(E+E)\otimes e$ system. The method has been extensively described in previous works, and we only provide a short summary here.

Each component of the doubly-degenerate ^3E state can interact via the Jahn-Teller effect, and the closely-spaced ^3E-states (shown in Fig. 3b and Fig. 4b in the main text) can interact via the pseudo Jahn-Teller effect. Thus, we build an effective Hamiltonian $\hat{H}$ that accounts for both of these effects up to the sixth order. To do so, we expand the elements of $\hat{H}$ in a Taylor series up to the sixth order along the e_x and e_y phonon modes (i.e., along x and y directions in real space). To identify the non-vanishing terms of the expansion coefficients, we use the fact that $\hat{H}$ must be invariant under the symmetry operations $\hat{S}$ of the C_{4v} point group, since $[\hat{H},\hat{S}]=0$. The symmetry operations $\hat{S}$ are given in Supplementary Table 5, namely, $\hat{C_4}$ (rotation by $\pi/2$), $\hat{C_2}$ (rotation by π), $\hat{\sigma_v}$ (reflection on mirror plane along C_4 axis), and $\hat{\sigma_d}$ (reflection along diagonal plane).

By doing this, we get the matrix

$$\hat{H}=\frac{1}{2}\sum_{n=0}^{6}\frac{1}{n!}\left\{\begin{pmatrix} V_1^{(n)}+W_{JT,1}^{(n)} & M_{JT,1}^{(n)} & Z_{PJT,1}^{(n)}+P_{PJT,1}^{(n)} & Z_{PJT,2}^{(n)}+P_{PJT,2}^{(n)} \\ M_{JT,1}^{(n)} & V_1^{(n)}-W_{JT,1}^{(n)} & -Z_{PJT,2}^{(n)}+P_{PJT,2}^{(n)} & Z_{PJT,1}^{(n)}-P_{PJT,1}^{(n)} \\ Z_{PJT,1}^{(n)}+P_{PJT,1}^{(n)} & -Z_{PJT,2}^{(n)}+P_{PJT,2}^{(n)} & V_2^{(n)}+W_{JT,2}^{(n)} & M_{JT,2}^{(n)} \\ Z_{PJT,2}^{(n)}+P_{PJT,2}^{(n)} & Z_{PJT,1}^{(n)}-P_{PJT,1}^{(n)} & M_{JT,2}^{(n)} & V_2^{(n)}-W_{JT,2}^{(n)} \end{pmatrix}\right\}$$

The explicit equations are as follows

$$V_1^{(0)} = a_1^{(0)} \tag{1}$$

$$V_1^{(2)} = a_1^{(2)}[x^2 + y^2] \tag{2}$$

$$\begin{aligned} V_1^{(4)} &= a_1^{(4)}[2x^4 - 12x^2y^2 + 2y^4] \\ &\quad + a_2^{(4)}[x^4 + 2x^2y^2 + y^4] \end{aligned} \tag{3}$$

$$\begin{aligned} V_1^{(6)} &= a_1^{(6)}[2x^6 - 10x^4y^2 - 10x^2y^4 + 2y^6] \\ &\quad + a_2^{(6)}[x^6 + 3x^4y^2 + 3x^2y^4 + y^6] \end{aligned} \tag{4}$$

$$V_2^{(0)} = b_1^{(0)} \tag{5}$$

$$V_2^{(2)} = b_1^{(2)}[x^2 + y^2] \tag{6}$$

$$\begin{aligned} V_2^{(4)} &= b_1^{(4)}[2x^4 - 12x^2y^2 + 2y^4] \\ &\quad + b_2^{(4)}[x^4 + 2x^2y^2 + y^4] \end{aligned} \tag{7}$$

$$\begin{aligned} V_2^{(6)} &= b_1^{(6)}[2x^6 - 10x^4y^2 - 10x^2y^4 + 2y^6] \\ &\quad + b_2^{(6)}[x^6 + 3x^4y^2 + 3x^2y^4 + y^6] \end{aligned} \tag{8}$$

$$W_{JT,1}^{(2)} = \lambda_1^{(2}[2x^2 - 2y^2] \tag{9}$$

$$W_{JT,1}^{(4)} = \lambda_1^{(4)}[2x^4 - 2y^4] \tag{10}$$

$$\begin{aligned} W_{JT,1}^{(6)} &= \lambda_1^{(6)}[2x^6 - 30x^4y^2 + 30y^4x^2 - 2y^6] \\ &\quad + \lambda_2^{(6)}[2x^6 + 2x^4y^2 - 2y^4x^2 - 2y^6] \end{aligned} \tag{11}$$

$$W_{JT,2}^{(2)} = \tau_1^{(2)}[2x^2 - 2y^2] \tag{12}$$

$$W_{JT,2}^{(4)} = \tau_1^{(4)}[2x^4 - 2y^4] \tag{13}$$

$$\begin{aligned} W_{JT,2}^{(6)} &= \tau_1^{(6)}[2x^6 - 30x^4y^2 + 30y^4x^2 - 2y^6] \\ &\quad + \tau_2^{(6)}[2x^6 + 2x^4y^2 - 2y^4x^2 - 2y^6] \end{aligned} \tag{14}$$

$$M_{JT,1}^{(2)} = \sigma_1^{(2)}[4xy] \tag{15}$$

$$M_{JT,1}^{(4)} = \sigma_1^{(4)}[4xy^3 + 4x^3y] \tag{16}$$

$$\begin{aligned} M_{JT,1}^{(6)} &= \sigma_1^{(6)}[12x^5y - 40x^3y^3 + 12xy^5] \\ &\quad + \sigma_2^{(6)}[4x^5y + 8x^3y^3 + 4xy^5] \end{aligned} \tag{17}$$

$$M_{JT,2}^{(2)} = \theta_1^{(2)}[4xy] \tag{18}$$

$$M_{JT,2}^{(4)} = \theta_1^{(4)}[4xy^3 + 4x^3y] \tag{19}$$

$$\begin{aligned} M_{JT,2}^{(6)} &= \theta_1^{(6)}[12x^5y - 40x^3y^3 + 12xy^5] \\ &\quad + \theta_2^{(6)}[4x^5y + 8x^3y^3 + 4xy^5] \end{aligned} \tag{20}$$

$$Z_{PJT,1}^{(0)} = c_1^{(0)} \tag{21}$$

$$Z_{PJT,1}^{(2)} = c_1^{(2)}[x^2 + y^2] \tag{22}$$

$$\begin{aligned} Z_{PJT,1}^{(4)} &= c_1^{(4)}[2x^4 - 12x^2y^2 + 2y^4] \\ &\quad + c_2^{(4)}[x^4 + 2x^2y^2 + y^4] \end{aligned} \tag{23}$$

$$\begin{aligned} Z_{PJT,1}^{(6)} &= c_1^{(6)}[2x^6 - 10x^4y^2 - 10x^2y^4 + 2y^6] \\ &\quad + c_2^{(6)}[x^6 + 3x^4y^2 + 3x^2y^4 + y^6] \end{aligned} \tag{24}$$

$$P_{PJT,1}^{(2)} = \eta_1^{(2)}[2x^2 - 2y^2] \tag{25}$$

$$P_{PJT,1}^{(4)} = \eta_1^{(4)}[2x^4 - 2y^4] \tag{26}$$

$$\begin{aligned} P_{PJT,1}^{(6)} &= \eta_1^{(6)}[2x^6 - 30x^4y^2 + 30x^2y^4 - 2y^6] \\ &\quad + \eta_2^{(6)}[2x^6 + 2x^4y^2 - 2x^2y^4 - 2y^6] \end{aligned} \tag{27}$$

$$Z_{PJT,2}^{(2)} = \mu_1^{(2)}[4xy] \tag{28}$$

$$Z_{PJT,2}^{(4)} = \mu_1^{(4)}[4xy^3 + 4x^3y] \tag{29}$$

$$\begin{aligned} Z_{PJT,2}^{(6)} &= \mu_1^{(6)}[12x^5y - 40x^3y^3 + 12xy^5] \\ &\quad + \mu_2^{(6)}[4x^5y + 8x^3y^3 + 4xy^5] \end{aligned} \tag{30}$$

$$P_{PJT,2}^{(4)} = d_1^{(4)}[8x^3y - 8xy^3] \tag{31}$$

$$P_{PJT,2}^{(6)} = d_1^{(6)}[8x^5y - 8xy^5] \tag{32}$$

The vibronic coupling parameters were determined by fitting the eigenvalues of $\hat{H}$ to the TDDFT-DDH single-point energies of the first ^3E excited state along the e_x and e_y phonon modes (i.e., to the CCD as obtained in the previous section). Note that we tried fitting the APES with expansions of only up to two- and four-orders, but the fit was poor. The fits with two-, four-, and six- orders are given in Supplementary Figure 4. Moreover, it is indeed expected that the strong vibronic coupling observed in our system requires higher order coupling parameters to fit the APES.

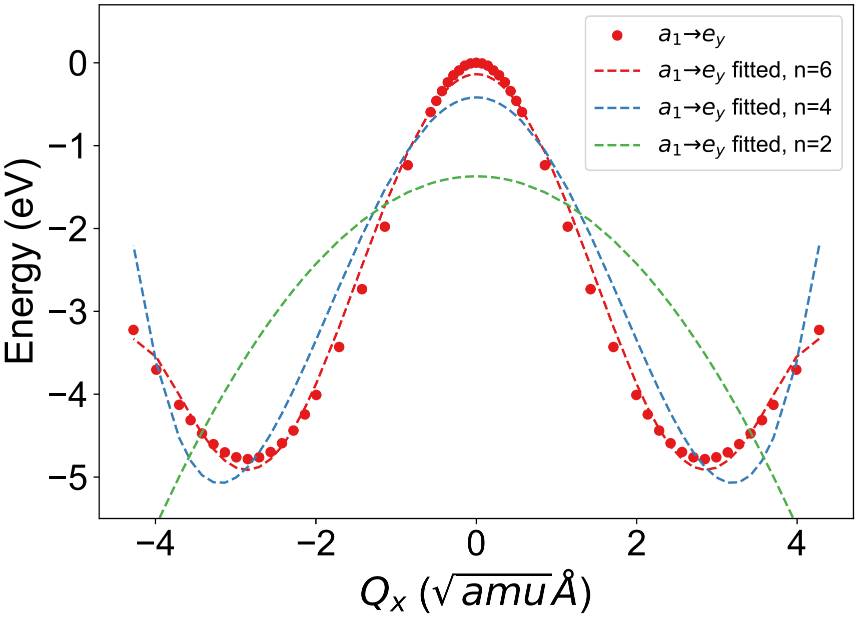

Supplementary Figure 4: Adiabatic potential energy surface of first ^3E-excited state along the e_x-phonon mode obtained with expansions of two-, four- and six-orders. The markers denote energies obtained at each configuration using single-point DDH (TDDFT-DDH) calculations.

The fitting procedure up to the sixth order is challenging, due to the large number of unknown parameters. Thus, while solving for the coupling parameters, we made several approximations:

1. We assume $a_{1,2}^{(n)} = b_{1,2}^{(n)}$, for $n > 0$ (i.e. non-coupling coefficients for different excited ^3E states are the same).

2. We found that including Jahn-Teller terms did not reduce the fitting error; i.e. in this system, the pseudo Jahn-Teller effect is dominant. Thus, we set $\lambda_{1,2}^{(n)} = \tau_{1,2}^{(n)} = \sigma_{1,2}^{(n)} = \theta_{1,2}^{(n)} = 0$.

3. We set $\mu_{1,2}^{(n)}$, $d_{1,2}^{(n)} = 0$, since these are coefficients of terms involving products of x and y, which will be 0 since we project the APES along either the x-axis ($y = 0$) or the y-axis ($x = 0$).

4. We assume only 2 excited states interact (i.e.we consider only a two-level pseudo Jahn-Teller effect instead of a multi-level pJT effect), and we fit only to the energies of the first excited state. Accounting for multi-level pJT would further increase the matrix size, leading to a larger number of unknown parameters.

These approximations helped reduce the number of unknown parameters while still retaining a realistic physical representation of the problem. Moreover, given the complicated loss function that needed to be minimized, we tested the influence of different initial parameters. We also tested for overfitting by fitting the curves using 80% of the data points, and calculating the error on the remaining 20% data points. We consistently found the effective phonon frequency to be around 20 meV and vibronic coupling parameters to be 20-500 meV. The vibronic coupling coefficients are given in Supplementary Table 7.

Supplementary Table 7: Non-coupling and pseudo Jahn Teller (pJT) coupling coefficients (meV)

Non-coupling coefficient	**Value (meV)**	**pJT coupling coefficient**	**Value (meV)**
$a_1^{(0)}$	-274.62	$c_1^{(2)}$	17.71
$a_1^{(2)}$	25.81	$c_1^{(4)}$	6.76
$a_1^{(4)}$	9.50	$c_2^{(4)}$	-16.47
$a_2^{(4)}$	-10.99	$c_1^{(6)}$	7.61
$a_1^{(6)}$	29.62	$c_2^{(6)}$	-14.77
$a_2^{(6)}$	29.24	$\eta_1^{(2)}$	448.57
$b_1^{(0)}$	-274.61	$\eta_1^{(4)}$	-70.93
		$\eta_1^{(6)}$	26.68
		$\eta_2^{(6)}$	26.68

Supplementary Note 8. Ground state phonon modes

We calculated the phonon modes for the NV^- defect at the ground state using the frozen phonon approach as implemented in the Phonopy package [8, 9]. The displaced configurations of the 216-atom supercell were generated using a displacement of 0.01 Åfrom the ground state, and the self-consistent calculations were carried out using the DDH functional (with a plane-wave cutoff of 80 Ry and Γ-point sampling).

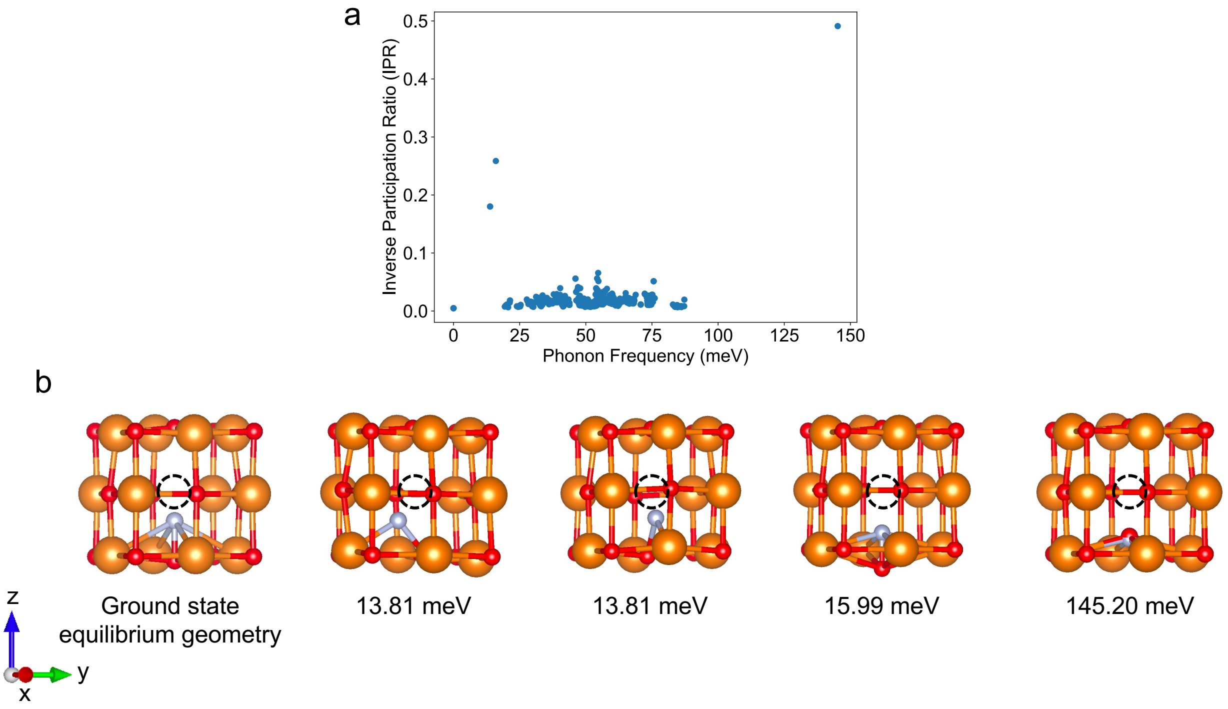

Supplementary Figure 5: a. Inverse participation ratio of phonon eigenvectors calculated using the DDH functional in a 216-atom supercell. **b.** Atomic displacements associated with the localized phonon modes. Only atoms near the defect are shown for clarity.

Supplementary Figure 5a shows the inverse participation ratio of the computed phonon modes. We note that there are four localized modes: a two-fold degenerate mode at 13.81 meV, a non-degenerate mode at 15.99 meV, and another non-degenerate mode at 145.20 meV. Supplementary Figure 5b shows the reference ground state structure and the displacements associated with the four localized phonon modes. We note that the modes are largely localized near the NV^- defect. The mode at 13.81 meV is an *e*-mode, at 15.99 meV is an

a_1-mode. The high energy mode at 145.20 meV corresponds to the N-O stretching mode (this value is similar to that of the stretching mode of the NO molecule, 232 meV [10]).

While the spin-phonon coupling function would have to be calculated to identify which phonon modes couple with the NV^- defect [11], given that the phonon energies generally exceed the zero-field splitting of this defect (46 GHz, i.e., 0.190 meV, at the DDH level), the spin relaxation time T_1 might be limited by the slower two-phonon processes as opposed to one-phonon direct and Orbach relaxation mechanisms. This could be favorable for the defect's T_1 value.

Supplementary Note 9. Strain tests

To identify which strain regime could be favorable in reducing the vibronic coupling, we carried out ΔSCF calculations (total energy differences with different occupation numbers) at the PBE level for a 4x4x4 supercell, with 120 Ry plane-wave cutoff. Note that from the defect configuration shown in Fig.3a of the main text, x- and y-directions are equivalent.

Supplementary Table 8: Effect of uniaxial strain on the optical properties of the NV^- center in MgO, calculated using ΔSCF-PBE.

Property	0%	-1% along x	-1% along z
Absorption (eV)	3.57	3.52	3.63
Emission (eV)	1.55	1.59	1.57
ZPL (eV)	2.45	2.50	2.48
ΔQ (amu$^{0.5}$Å)	3.37	3.15	3.47

For the uniaxial strain case, we first strained the unit cell by 1% (compressive) along the x-direction and relaxed the structure by allowing the lattice parameters along y- and z-directions to relax. We then created a 4x4x4 supercell with the defect and the new lattice parameters. Similarly, we strained the unit cell by 1% (compressive) along the z-direction and relaxed the structure by allowing the lattice parameters along the x- and y-directions to be optimized, and then created a 4x4x4 supercell with the defect and the new lattice parameters.

Supplementary Table 9: Effect of biaxial strain on the optical properties of the NV^- center in MgO, calculated using ΔSCF-PBE.

Property	0%	-4% along xz	-1% along xy
Absorption (eV)	3.57	3.60	3.47
Emission (eV)	1.55	1.50	1.87
ZPL (eV)	2.45	2.27	2.70
ΔQ (amu$^{0.5}$Å)	3.37	4.44	2.26

For the biaxial strain case, we first compressively strained the unit cell by 4% (1%) along the xz (xy) plane and optimized the structure by allowing the lattice parameters along the y- (z-) direction to vary. We then created a 4x4x4 supercell with the defect and the new lattice parameters.

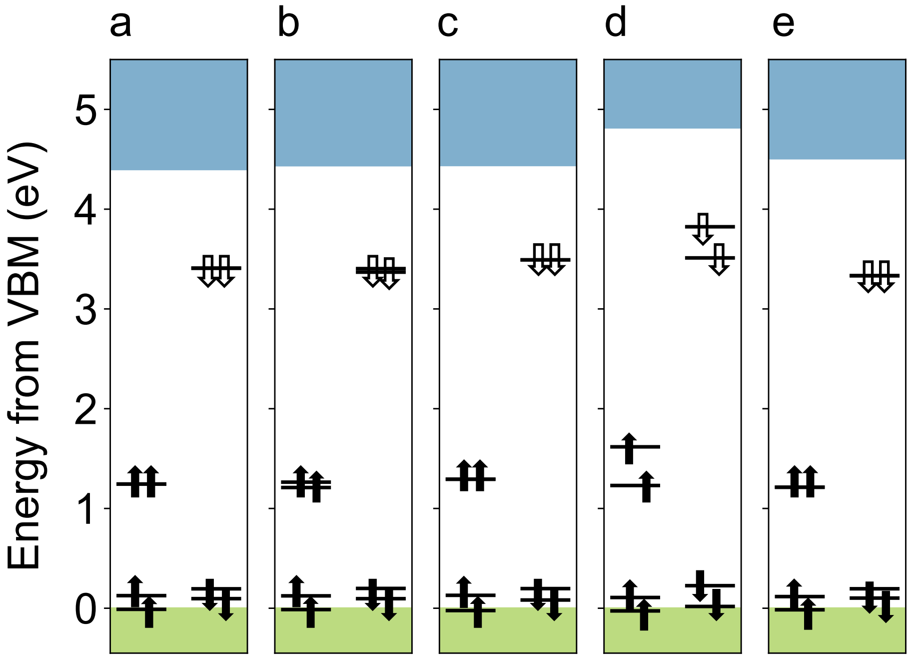

Supplementary Figure 6: Defect level diagram of the NV^{-} center in MgO under different strain cases, calculated at the PBE level. **(a)** unstrained **(b)** -1% along x **(c)** -1% along z **(d)** -4% along xz **(e)** -1% along xy

Note that we also considered the effect of tensile strain, but we faced convergence issues with the ΔSCF method. However, it is unlikely that tensile strain will help reduce vibronic coupling. For example, in our test for 1% biaxial tensile strain along the xy-plane, the partially optimized structure in the excited state had a ΔQ of 4.44 amu$^{0.5}$Å.

Supplementary Table 8 and Supplementary Table 9 list the effect of these different strain configurations on the optical transitions energies of the NV^{-} defect in MgO. Supplementary Figure 6 shows the effect of strain on the Kohn-Sham defect levels of the NV^{-} center in MgO.

Supplementary Note 10. Convergence tests for plane-wave cutoff energies

We determined our plane-wave cutoff energy based on the convergence of the energy difference between the e-state in the spin up channel and the valence band maximum for the 216-atom supercell with the NV^- defect. Calculations were done at the Γ-point with the DDH functional. As seen in Supplementary Figure 7, the energy difference is converged to 0.6 meV with a cutoff energy of 80 Ry, and to 7 meV when the cutoff energy is 60 Ry. Therefore, we use 80 Ry for our DFT-DDH calculations, and 60 Ry for the more expensive TDDFT-DDH calculations. Note that the small differences in energy (10^{-4} eV) beyond a plane-wave cutoff of 90 Ry are due to differences in convergence of the self-consistency cycle.

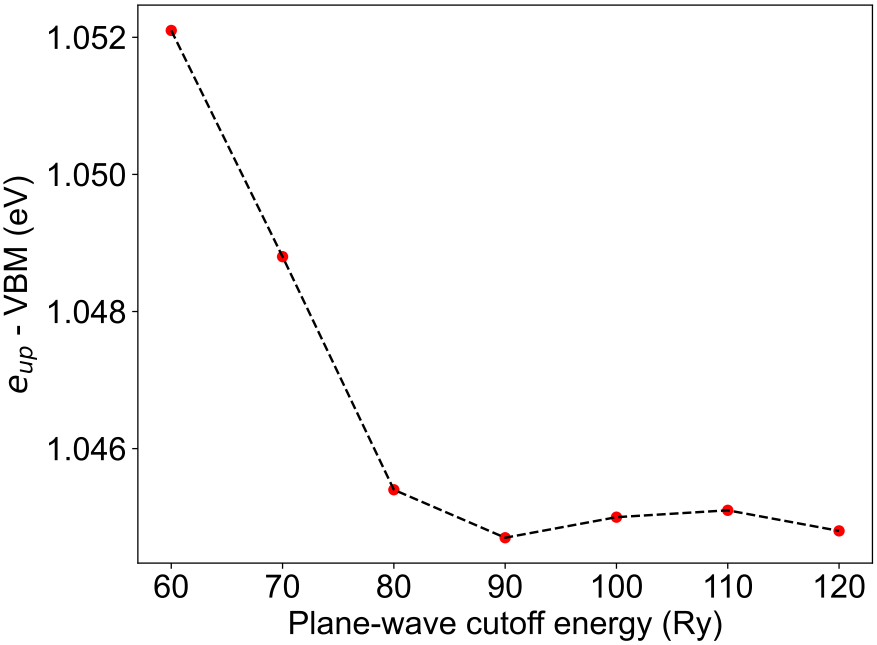

Supplementary Figure 7: Energy difference between the e-state in the spin up channel and the valence band maximum as a function of plane-wave cutoff energy.

Supplementary Note 11. Experimental vs. DDH lattice constants

We computed the equilibrium DDH lattice constant by fitting the total energies of the 8-atom unit cell of MgO at different lattice constants to the Murnaghan equation of state [12]. A plane-wave cutoff of 80 Ry was used, and the Brillouin zone was sampled with a 6 x 6 x 6 k-point mesh. The fit is shown in Supplementary Figure 8. We obtained the DDH lattice constant to be 4.195 Å, in close agreement with the experimental value of 4.19 Å.

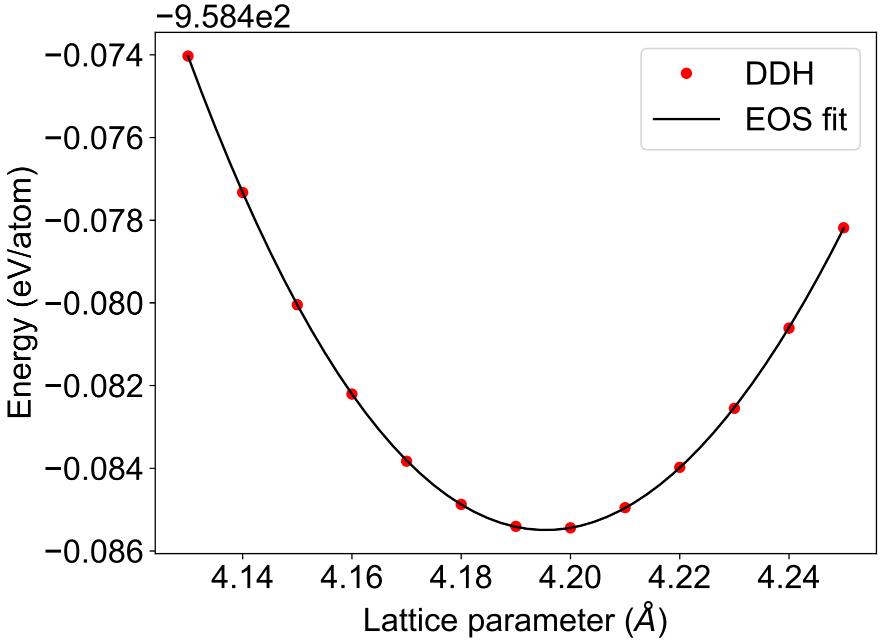

Supplementary Figure 8: Total energy vs. lattice parameter for MgO unit cell and the corresponding equation of state fit.

Supplementary Note 12. Calculation of O_2 and N_2 chemical potentials

We used the HSE functional [13] to obtain E_{DFT,O_2} and E_{DFT,N_2}. Calculations of E_{DFT,O_2} and E_{DFT,N_2} were done in a cubic box of side length 12.57 Å, plane-wave cutoff of 80 Ry, and with Γ-point sampling. As seen in Supplementary Table 10, the HSE-computed binding energy and bond length of the respective molecules match most closely with experiments.

Supplementary Table 10: Binding energy and bond length of O_2 and N_2 with different exchange correlation functionals.

Quantity	DDH (α=0.34)	HSE	PBE0	Experiment
O_2 binding energy (eV)	-4.39	-5.14	-5.13	-5.12 [14, 15]
O_2 bond length (Å)	1.186	1.194	1.194	1.208 [16]
N_2 binding energy (eV)	-9.10	-9.34	-9.33	-9.76 [14, 15]
N_2 bond length (Å)	1.085	1.084	1.089	1.098 [16]

Supplementary Note 13. Defect formation energies using PBE vs. DDH functional

PBE is less accurate than hybrid exchange-correlation functionals for calculating defect formation energies. However, performing hybrid calculations for all the 3000 defects is computationally prohibitive. Moreover, while PBE systematically underestimates the formation energies, band gaps, etc., it still follows the general trends obtained using hybrid functionals. To check this, we compared the defect formation energies of the NV defect in MgO as a function of Fermi level at both the PBE and DDH level (Supplementary Figure 9). We see that while the band gap and formation energies are underestimated with PBE (as expected), the relative widths of the stability regions of the different charge states are nearly identical. PBE also predicts the ground state of NV$^-$ to be a spin triplet, same as DDH. Thus, using PBE for screening purposes in this system (especially since there are no d- or f-elements involved), is valid.

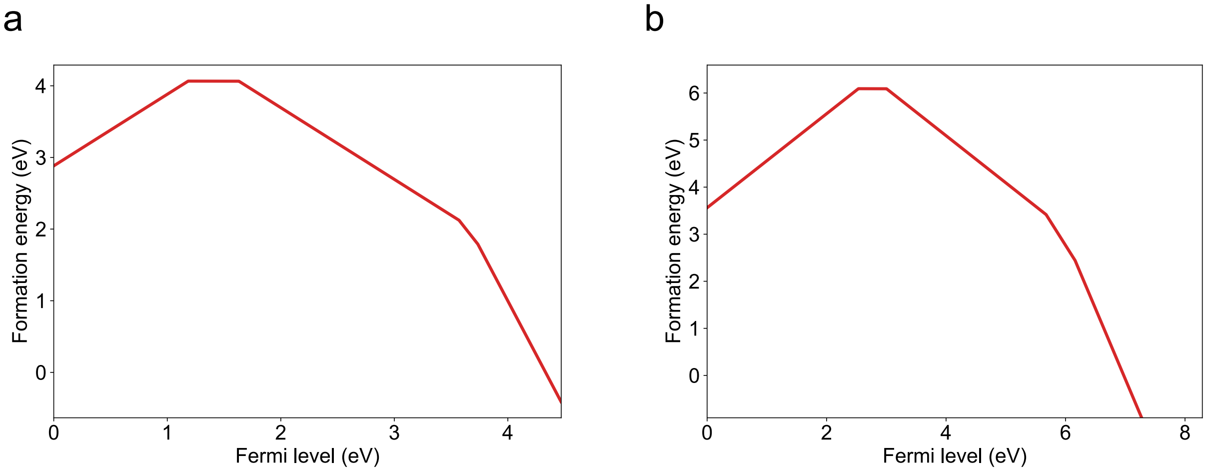

Supplementary Figure 9: Defect formation energies of the NV defect in MgO as a function of Fermi level using **a.** PBE **b.** DDH exchange correlation functionals. The slope of the line corresponds to the charge state of the defect.

[1] R. Whited, C. J. Flaten, and W. Walker, Exciton thermoreflectance of mgo and cao, Solid State Communications **13**, 1903 (1973).

[2] D. Wing, G. Ohad, J. B. Haber, M. R. Filip, S. E. Gant, J. B. Neaton, and L. Kronik, Band gaps of crystalline solids from wannier-localization–based optimal tuning of a screened range-separated hybrid functional, Proceedings of the National Academy of Sciences **118**, e2104556118 (2021).

[3] G. Henkelman, B. P. Uberuaga, and H. Jónsson, A climbing image nudged elastic band method for finding saddle points and minimum energy paths, The Journal of chemical physics **113**, 9901 (2000).

[4] M. Pesci, F. Gallino, C. Di Valentin, and G. Pacchioni, Nature of defect states in nitrogen-doped mgo, The Journal of Physical Chemistry C **114**, 1350 (2010).

[5] H. H. Claassen, C. L. Chernick, and J. G. Malm, *Vibrational spectra and structures of XeF4 and XeOF4*, Tech. Rep. (Argonne National Lab., Ill.; Argonne National Lab.(ANL), Argonne, IL (United . . . , 1963).

[6] A. Viel and W. Eisfeld, Effects of higher order jahn-teller coupling on the nuclear dynamics, The Journal of chemical physics **120**, 4603 (2004).

[7] W. Eisfeld and A. Viel, Higher order (a+ e) $\otimes$ e pseudo-jahn–teller coupling, The Journal of chemical physics **122** (2005).

[8] A. Togo, First-principles phonon calculations with phonopy and phono3py, Journal of the Physical Society of Japan **92**, 012001 (2023).

[9] A. Togo, L. Chaput, T. Tadano, and I. Tanaka, Implementation strategies in phonopy and phono3py, Journal of Physics: Condensed Matter **35**, 353001 (2023).

[10] J. Laane and J. R. Ohlsen, Characterization of nitrogen oxides by vibrational spectroscopy, Progress in inorganic chemistry , 465 (1980).

[11] S. Mondal and A. Lunghi, Spin-phonon decoherence in solid-state paramagnetic defects from first principles, npj Computational Materials **9**, 120 (2023).

[12] C.-L. Fu and K.-M. Ho, First-principles calculation of the equilibrium ground-state properties of transition metals: Applications to nb and mo, Physical Review B **28**, 5480 (1983).

[13] A. V. Krukau, O. A. Vydrov, A. F. Izmaylov, and G. E. Scuseria, Influence of the exchange screening parameter on the performance of screened hybrid functionals, The Journal of chemical physics **125** (2006).

[14] J. A. Pople, M. Head-Gordon, D. J. Fox, K. Raghavachari, and L. A. Curtiss, Gaussian-1 theory: A general procedure for prediction of molecular energies, The Journal of Chemical Physics **90**, 5622 (1989).

[15] T. C. Allison, NIST-JANAF Thermochemical Tables - SRD 13 (2024), accessed: 2024-11-15.

[16] K.-P. Huber, Constants of diatomic molecules, Molecular spectra and molecular structure **4**, 146 (1979).